PHYSICAL REVIEW FLUIDS **7**, 064201 (2022)

Active control of particle position by boundary slip in inertial microfluidics

Chengliang Xuan, Weiyin Liang, Bing He,[*] and Binghai Wen[†]
Guangxi Key Lab of Multi-Source Information Mining & Security, Guangxi Normal University,
Guilin 541004, China
and School of Computer Science and Engineering, Guangxi Normal University, Guilin 541004, China

(Received 20 January 2022; accepted 31 May 2022; published 13 June 2022)

Inertial microfluidics is able to focus and separate particles in microchannels based on the characteristic geometry and intrinsic hydrodynamic effect. Yet, the vertical positions of suspended particles in the microchannel cannot be manipulated in real time. In this study, we utilize the boundary slip effect to regulate the parabolic velocity distribution of fluid in the microchannel and present a scheme to actively control the vertical positions of particles in inertial microfluidics. The flow field of a microchannel with a unilateral slip boundary is equivalent to that of the microchannel widened by the relevant slip length, and the particle equilibrium positions in the two microchannels are consistent consequently. Then, we simulate the lateral migrations of three kinds of typical particles, namely, circular, elliptical, and rectangular in the microchannel. Unlike the smooth trajectories of circular particles, the motions of the elliptical and rectangular particles are accompanied by regular fluctuations and nonuniform rotations due to their noncircular geometries. The results demonstrate that the unilateral slip boundary can effectively manipulate the vertical equilibrium positions of particles. The present scheme can improve the accuracy and flexibility of particulate focusing, separating, and transport in inertial microfluidics.

DOI: 10.1103/PhysRevFluids.7.064201

I. INTRODUCTION

Microfluidics concerns the manipulation of fluids in channels with dimensions of tens to hundreds of micrometers. It has emerged in recent years as a distinct new area of research thanks to its application in many diverse fields, such as chemistry, biology, medicine, and physics [1–7]. Nowadays, several technologies have already been proposed and developed to manipulate particles in microfluidic systems. According to the source of the manipulating forces, these technologies can be categorized as active and passive types. Active technologies rely on external force fields, whereas passive technologies depend entirely on the channel geometry or intrinsic hydrodynamic forces. As a passive technology, inertial microfluidic is used for particle focusing [8], sorting [9], and enriching [10] in industry, biology, and medicine. The finite inertial of the fluid brings about several intriguing inertial effects that form the basis of inertial microfluidics, including inertial migration and secondary flow. Inertial migration is inspired by a natural phenomenon that randomly dispersed particles in a channel flow migrate spontaneously and laterally to several equilibrium positions after traveling a sufficiently long distance. As early as the 1960s, Segré and Silberberg found that suspended spherical particles in a pipe flow would migrate laterally away from the wall and finally reach a certain lateral equilibrium position [11]. The phenomenon was called the Segré–Silberberg effect later and can also be observed for other shaped particles, such as cylinder, ellipse, disk, rod,

---

[*] hebing@gxnu.edu.cn
[†] oceanwen@gxnu.edu.cn

biconcave particles, etc. Until 2007, Di Carlo *et al.* [12] performed the inertial focusing of particles at a micro–scale. In a pipe with a diameter of the order of microns, the length of pipe required for particles to reach the equilibrium state was reduced to centimeters or even millimeters. The inertial migration of particles has now been practically applied in microfluidics.

Different focusing and separation effects were achieved through microchannels with different structures. The microchannel structure is the important parameter that determines the functionality and performance of inertial microfluidic devices. Ramachandraiah *et al.* [13] used U-shaped and S-shaped microchannels to achieve the focusing of particles and found that the focusing position of particles is independent of the radius of curvature. Bhagat *et al.* [14] used a 10-loop spiral microchannel to achieve three-dimensional (3D) focusing of fluorescently labeled 6 μm particles without any additional sheath fluids. Sun *et al.* [15] proposed a passive double spiral microfluidic device to continuously and efficiently separate and enrich tumor cells from diluted whole blood. Zhang *et al.* [16] carefully evaluated the effect of particle centrifugal force on particle focusing and demonstrated for the first time that a single focusing streak can be achieved in a symmetric serpentine microchannel. Ciftlik *et al.* [17] used a channel with 10 μm × 16 μm cross-section and the length of 8.8 mm to successfully focus particles with the diameter of 2 μm. The Reynolds number in the system could be changed between 75 to 1500, thus their microfluidics obtained high throughput.

At the same time, when the characteristic length of the flow field goes to a micron/nanometer, the interaction between the fluid and the wall must be considered. As a result, the boundary slip will occur at the wall and it has an important effect on the fluid field at the micro-nano scale [18]. To quantify the boundary slip, Navier [19] proposed the concept of "slip length," which is defined as the distance inside the wall at which the extrapolated fluid velocity would be equal to the velocity of the wall [20]. Several studies about the effect of the boundary slip have also been reported [21,22]. Li *et al.* [21] studied the effect of nanobubbles on the slippage experimentally and theoretically. In a 5 μm × 5 μm area, they found an increase from 8 to 512 nm in slip length by increasing the surface coverage of nanobubbles from 1.7% to 50.8% and decreasing the contact angle of nanobubbles from 42.8° to 16.6°. Their results indicate that nanobubbles can always act as a lubricant and significantly increase the slip length. Minakov *et al.* [22] studied the flow regimes and mixing performance in a T-type micromixer at high Reynolds numbers. They found that the flow regimes and the efficiency of mixing can be changed by using the slip boundary conditions. Schäffel *et al.* [23] reported that the slip length of water on a microstructured superhydrophobic surface was close to 100 microns. Lee *et al.* [24,25] showed that the slip lengths of water on the surfaces with posts and grates of micro-nano structures were up to 140 and 400 microns, respectively.

Many studies have focused on inertial microfluidics by numerical method. In particular, the lattice Boltzmann method (LBM), as a reliable computational fluid dynamics method, is widely used for the numerical simulation of microfluidics [26–32]. Sun *et al.* [27] studied the particle focusing in a three–dimensional rectangular channel with the lattice Boltzmann method. Huang *et al.* [28] used a multi-relaxation-time lattice Boltzmann method to study the rotation of a spherical particle in a Couette flow. They found seven periodic and steady rotation modes for a prolate spheroid. Wen *et al.* [29,30] simulated the migration of biconcave particles in straight channels and made a positive contribution to the study of blood circulation of birds with elliptical red blood cells. Liu *et al.* [31] carried out a three-dimensional numerical simulation of the movement of particles in a serpentine microchannel and proposed a fitting formula for the inertial lift on a sphere drawn from DNS data obtained in straight channels. However, there is no method to control particles' equilibrium positions in real time in inertial microfluidic.

In this paper, the slip boundary condition is used on the side of the Poiseuille flow. The velocity distribution of the flow field is controlled by adjusting the slip length, so as to control the equilibrium positions of particles. The simulation results show that this method can control the target particles more accurately and the equilibrium positions can be adjusted in real time. In addition, this method is very simple and robust. The structure of this paper is as follows. In Sec. II, we briefly describe the lattice Boltzmann method. Section III is devoted to describing the slip boundary condition, derivation, and verification of the slip length formula. The effect of boundary slip on the migration trajectory of different particles is presented in detail in Sec. IV. Section V concludes the paper.

II. NUMERICAL METHOD

To analyze the effect of the boundary slip, the lattice Boltzmann method with single relaxation time is used for simulating Poiseuille flow. To precisely describe the motion of particles with different shapes, the moving particle boundary is treated by the quadratic interpolation and the hydrodynamic force is calculated by the Galileo invariant momentum exchange method [33,34].

Nowadays, the lattice Boltzmann method has developed into an alternative and promising numerical scheme for simulating complex fluid flows [35,36]. Compared with other traditional numerical methods, this method combines the advantages of the macroscopic model and the molecular dynamics model. It has the advantages of a simple description of fluid interaction, easy setting of complex boundaries, easy parallel computing, and easy implementation of the program.

The lattice Boltzmann model with single relaxation time (SRT) can be written as [26,37,38]

$$\frac{\partial f_i}{\partial t}+\boldsymbol{e}_i\cdot\nabla f_i=-\frac{1}{\tau}\big(f_i-f_i^{(\mathrm{eq})}\big)\quad (i=0,1,2,\dots,N-1), \tag{1}$$

where $\boldsymbol{e}_i$ is a discrete velocity vector, f_i is the particle distribution function with the velocity $\boldsymbol{e}_i$, $f_i^{(\mathrm{eq})}$ is the corresponding equilibrium distribution function, N is the number of the different velocities in the model, and τ is the relaxation time. Equation (1) is discretized in space $\boldsymbol{x}$ and time t:

$$f_i(\boldsymbol{x}+\boldsymbol{e}_i\delta t,t+\delta t)-f_i(\boldsymbol{x},t)=-\frac{1}{\tau}\big[f_i(\boldsymbol{x},t)-f_i^{(\mathrm{eq})}(\boldsymbol{x},t)\big], \tag{2}$$

where δ_t is the time step. In the model on a square lattice in two dimensions (D2Q9), the discrete velocity set is $\boldsymbol{e}=\{(0,0),(1,0),(0,1),(-1,0),(0,-1),(1,1),(-1,1),(-1,-1),(1,-1)\}$ representing the nine directions, respectively. $f_i^{(\mathrm{eq})}(\boldsymbol{x},t)$ can be calculated by

$$f_i^{(\mathrm{eq})}(\boldsymbol{x},t)=\rho\omega_i\left[1+3(\boldsymbol{e}_i\cdot\boldsymbol{u})+\frac{9}{2}(\boldsymbol{e}_i\cdot\boldsymbol{u})^2-\frac{3}{2}\boldsymbol{u}^2\right], \tag{3}$$

where weight factors ω_i are given by $\omega_o=4/9$, $\omega_{1-4}=1/9$, $\omega_{5-8}=1/36$, ρ and $\boldsymbol{u}$ are the macroscopic density and the macroscopic velocity vector, respectively, are given by

$$\rho=\sum_i f_i\quad\text{and}\quad\boldsymbol{u}=\frac{1}{\rho}\sum_i\boldsymbol{e}_i f_i. \tag{4}$$

The lattice Boltzmann method applies two essential steps, collision and streaming, to reveal phenomena at the mesoscopic scale. During a time step, the particle distribution functions in a lattice site collide and then flow into its neighboring lattice sites [39]. Hence, the corresponding computations of Eq. (2) are performed as

$$\text{Collision}:\quad\tilde{f}_i(\boldsymbol{x},t)-f_i(\boldsymbol{x},t)=-\frac{1}{\tau}\big[f_i(\boldsymbol{x},t)-f_i^{(\mathrm{eq})}(\boldsymbol{x},t)\big], \tag{5}$$

$$\text{Streaming}:\quad f_i(\boldsymbol{x}+\boldsymbol{e}_i\delta x,t+\delta t)=\tilde{f}_i(\boldsymbol{x},t), \tag{6}$$

where f_i and $\tilde{f}_i$ denote precollision and postcollision states of the particle distribution functions, respectively. The dominant part of the computations, namely the collision step, is completely local, so the discrete equations are natural to parallelize.

III. REGULATING THE VELOCITY DISTRIBUTION BY BOUNDARY SLIP

The nature of the boundary condition for fluid flows past solid surfaces has been a subject of interest for a long time. The no-slip boundary condition, that is, the assumption that the velocity

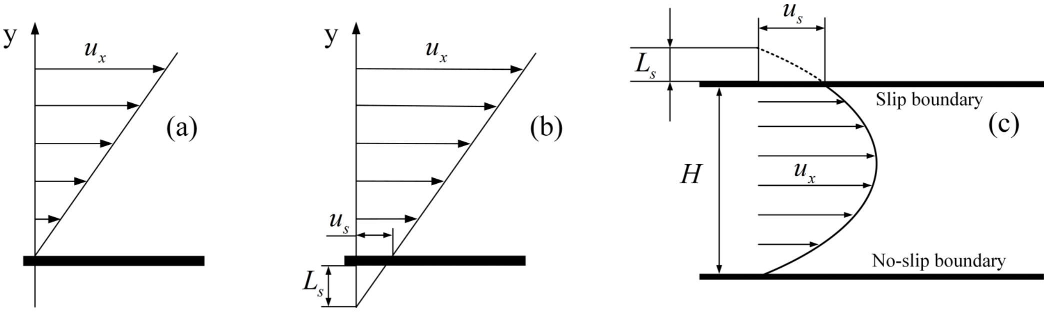

FIG. 1. Schematic diagrams of shear flows with (a) a no-slip boundary and (b) a slip boundary. (c) A channel flow with a slip upper boundary and a no-slip lower boundary. Owing to the boundary slip, the position of maximum velocity in the channel is moved toward the upper boundary, and the deformed parabolic velocity distribution is equivalent to that of the Poiseuille flow in a channel with width $H + L_s$.

of a liquid at a surface is always identical to the velocity of the surface, is extremely successful in describing macroscale viscous flows. However, at the nanoscale, this assumption is usually broken down [3]. Study shows that slip exists at the microscale and its value is significantly affected by surface and fluid characteristics [40]. Some early experiments that demonstrate slip boundary conditions mostly involve the flow of liquids through thin lyophobic capillaries [41,42]. Some new experiments using more modern technology have also shown evidence of boundary slip [43–45].

A. Slip boundary scheme

As early as 1823, Navier [19] proposed the linear slip boundary condition hypothesis, which assumes that the slip velocity is proportional to the local shear rate,

$$u_s = L_s \frac{\partial u_x}{\partial y}|_{\text{wall}}, \tag{7}$$

where u_s is the slip velocity on the boundary, L_s is the slip length and u_x is the tangential velocity of the fluid along the boundary surface. Figures 1(a) and 1(b) show the shear flow with a no–slip boundary and a slip boundary. When a channel flow has a slip upper boundary and a no–slip lower boundary, the velocity distribution of the flow field is shown in Fig. 1(c). In this paper, we adopt the scheme of the Fig. 1(c) to simulate the migration of particles.

In numerical simulations, boundary slip is usually implemented through boundary conditions. Especially, a kind of kinetic boundary conditions has been developed in LBM to simulate boundary slip phenomena effectively. Succi [46] proposed a combination of the bounce–back and specular reflection condition to capture slip velocity on the solid wall, which is denoted as the bounce–back specular reflection method or BSR method. Guo *et al.* [47] analyzed numerical error and discrete effect on the bounce–back and specular–reflection boundary condition and the Maxwellian boundary condition, and found that both schemes are virtually equivalent in principle. Chai *et al.* [48] proposed a new combination of bounce–back and full diffusive boundary conditions to investigate the incompressible gaseous flow in a microchannel with surface roughness. In this paper, we adopt the hybrid boundary condition proposed by Succi, which is simple, efficient, and has been widely applied.

As shown in Fig. 2, the distribution functions of f_2, f_5, f_6 for the grid need to be obtained according to the boundary conditions, others can be obtained according to the migration step. The hybrid boundary condition proposed by Succi combines the bounce–back (the blue lines) with the specular reflection (the red lines) based on the proportionality factor r. For the BSR method, the

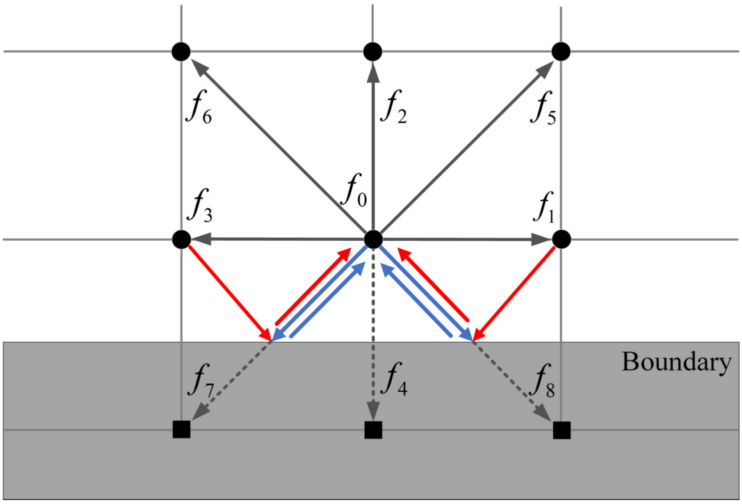

FIG. 2. Schematic diagram of the bounce–back specular reflection boundary condition. The boundary is located at the middle of the two rows of lattices, and the distribution functions to be solved are composed of the bounce–back and the specular reflection in a proportional factor r. The blue lines represent bounce–back and the red lines represent specular reflection.

unknown distribution functions are given by

$$\begin{cases} f_2 = f'_4 \\ f_5 = rf'_7 + (1-r)f'_8 + 2r\rho\omega_i c_5 \cdot \boldsymbol{u}_\omega / 2c_s^2 \\ f_6 = rf'_8 + (1-r)f'_7 + 2r\rho\omega_i c_6 \cdot \boldsymbol{u}_\omega / 2c_s^2 \end{cases}, \tag{8}$$

where f'_i is the distribution function of the node in the i direction after the collision, $\boldsymbol{u}_\omega$ is the velocity of the wall, r represents the proportion of bounce–back reflections in the interactions with the wall and $1 - r$ represents the proportion of specular reflections. Therefore, $r = 1$ corresponds to pure bounce–back reflection and $r = 0$ to pure specular reflection.

B. Slip length of Poiseuille flow

For the incompressible Newtonian fluid with constant viscosity, two–dimensional steady Poiseuille flow is carried out in the x direction between two infinite plates. If the continuity assumption is satisfied and the z direction is unlimited width, the Navier-Stokes equation in the Cartesian coordinate system can be simplified as

$$\frac{d^2u_x}{dy^2} = \frac{1}{\mu}\frac{dp}{dx}, \tag{9}$$

where μ is the viscosity of the fluid and p is the pressure.

As shown in Fig. 1(c), the lower boundary is no-slip $u_{x|y=0} = 0$, whereas the upper boundary has the slip velocity $u_{x|y=H} = u_s$. Substituting the two boundary conditions into Eq. (13) gives the velocity distribution in the vertical direction

$$u_x(y) = \frac{y}{H}u_s + \frac{1}{2\mu}\frac{dp}{dx}(y^2 - Hy), \tag{10}$$

where $y \in (0, H)$. The analytical solution of Poiseuille flow with flow field width $H + L_s$ is

$$u_x(y) = \frac{1}{2\mu}\frac{dp}{dx}(y^2 - Hy - L_s y). \tag{11}$$

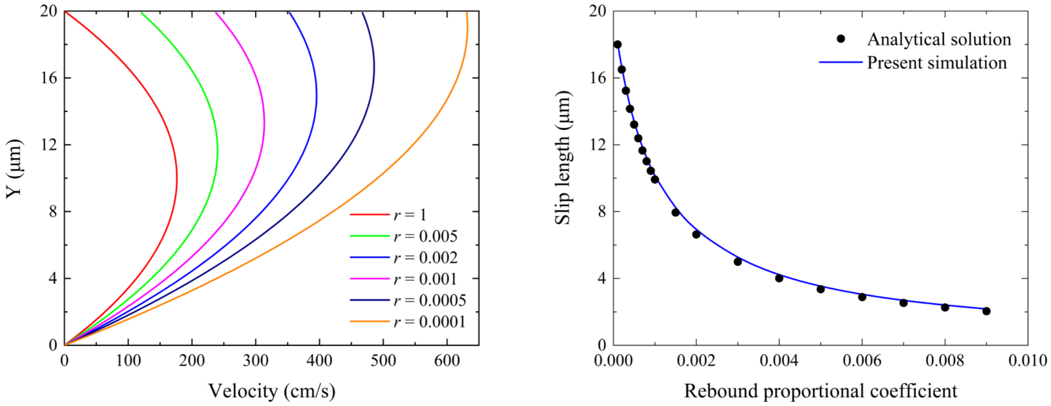

(a) (b)

FIG. 3. (a) The effect of boundary slip on velocity distribution of the channel flow at different rebound proportional coefficients r. (b) The slip lengths of the simulations with a series of rebound proportional coefficients are in agreement with the analytical solutions.

Based on Eq. (10) and the analytical solution Eq. (11), we can obtain the relationship between the slip length L_s and the slip velocity u_s:

$$L_s = -\frac{2\mu u_s}{H}\left(\frac{dp}{dx}\right)^{-1}. \tag{12}$$

Then, according to the definition of velocity $\rho u_j = c(f_1^j - f_3^j + f_5^j - f_6^j + f_8^j - f_7^j) + \frac{\delta_t}{2}\rho a$ and the stream law of particle distribution function, the relation formula of the flow velocity in the x direction between the adjacent mesh u_H and u_{H-1} can be obtained [47]:

$$u_{H-1} = \frac{1-2\tau+2r(\tau-2)}{1-2\tau+2r(\tau-1)}u_H + \frac{6(2\tau-1)+r(8\tau^2-20\tau+11)}{(2\tau-1)[1-2\tau+2r(\tau-1)]}\boldsymbol{a}, \tag{13}$$

where $\boldsymbol{a}$ is the external force. Considering the linear velocity distribution of the flow field, the external force $\boldsymbol{a}$ is 0. Eq. (13) can be simplified as

$$u_{H-1} = \frac{1-2\tau+2r(\tau-2)}{1-2\tau+2r(\tau-1)}u_H. \tag{14}$$

Substituting Eq. (10) and Eq. (12) into Eq. (14), we get the function of the slip length L_s, which is related to the rebound coefficient r.

$$L_s = \frac{(H-1)[1-2\tau+2r(\tau-1)]}{(1-2\tau)+2r(H-\tau+1)}. \tag{15}$$

C. Numerical verifications

In the above section, we introduced the slip boundary scheme and derived the relationship among the slip length, the slip velocity, and the rebound coefficient. In this subsection, the effectiveness of the BSR boundary condition in a horizontal channel is verified by the numerical experiment. The width H of the channel is 20 μm. The fluid density is 1 g/cm^3 and the kinematic viscosity coefficient is $\upsilon = 1 \times 10^{-6}$ m^2/s. BSR boundary condition is applied at the upper boundary of the channel wall and the half-way bounce-back boundary condition is applied at the lower boundary. As shown in Fig. 3(a), the different velocity distribution of the flow field can be obtained by changing the coefficient r in the slip boundary condition. When $r = 1$, the slip boundary condition is equal

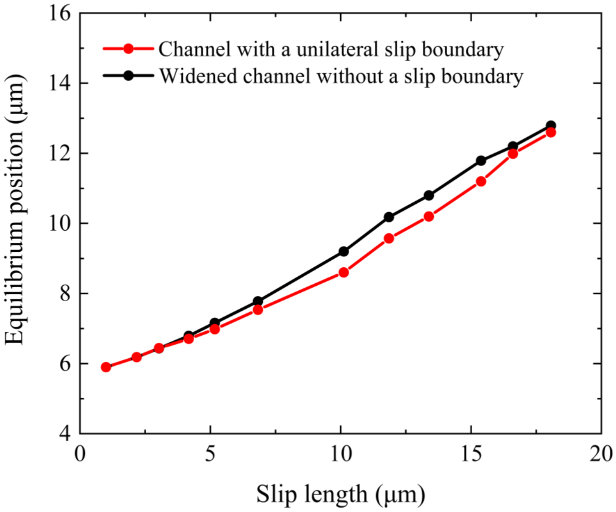

FIG. 4. The particle equilibrium positions in the channel with the width H and a unilateral slip length L_s agree very well with those in the channel widened to $H + L_s$ without a slip boundary.

to the half-way bounce-back boundary condition, so the velocity of the flow field is symmetric. As the coefficient r gradually decreases, the maximum velocity position of the flow field will gradually move toward the upper boundary, which is just like broadening the boundary of the flow field upward and the widened length is the slip length. The maximum velocity position of the flow field will only be infinitely close to the upper boundary but cannot exceed it. Also, the velocity of the flow field will become faster.

Then, to verify the correctness of the slip length formula in the previous section, the simulations with different rebound proportional coefficients are performed and the results are shown in Fig. 3(b). The solid line is the slip length simulated by changing the coefficient r of the BSR boundary condition. In this simulation, the slip length can reach 18 μm when the coefficient r is 1×10^{-4}. Similar slip lengths have been reported in studies [49,50]. The results are consistent with that derived by the analytical solution and indicate the proposed slip length formula is correct. This also confirms that it is feasible to adjust the slip length by using different rebound proportional coefficients.

To investigate the effect of boundary slip on the equilibrium position of the particle, a circular particle with a diameter of 4 lattice units, is added into the Poiseuille flow with slip boundary condition. Setting the boundary condition of the flow field, two cases are considered. The first one uses the slip boundary condition and sets different slip lengths L_s on the upper boundary, and the half-way bounce condition is applied on the lower boundary. In the second case, the half-way bounce condition is applied in the upper and lower boundaries, and the channel is widened to $H + L_s$. As shown in Fig. 4, the black line is the simulation of the first case, and the red is the result of the second case. The results show that the boundary slip causes the maximum velocity point of the flow field to move upward, so that the equilibrium position of the particles moves upward. The final equilibrium positions of circular particles are basically consistent. When the slip length is less than 6 μm, the equilibrium positions of the two cases fit perfectly. As the slip length grows from 8 to 16 μm, the difference in the equilibrium positions between the two cases is about 5%. When the slip length is large enough, the equilibrium position of the particle in the first case is relatively close to the upper wall. The main role of the wall is to slow down particles and keep them away from the wall, so the effect of the wall will be more obvious when the particle is nearer to the wall. Thus, the difference decreases again after the slip length exceeds 16 μm.

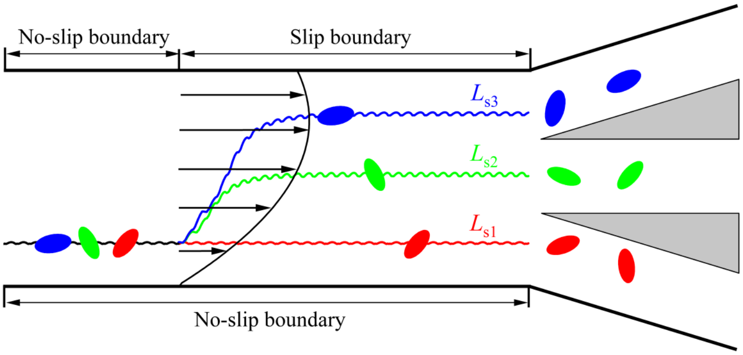

FIG. 5. Schematic diagram of active control of particle positions in inertial microfluidics. With the increasing slip length of the upper boundary, namely $L_{s3} > L_{s2} > L_{s1} = 0$, the particles can migrate to the different equilibrium positions in the vertical direction.

IV. ACTIVE CONTROL OF VERTICAL PARTICLE POSITIONS

From the above results, it can be found that the velocity distribution of the flow field can be changed by employing the slip boundary condition on the boundary of the Poiseuille flow. The change of velocity distribution in the flow field will affect the migration and the equilibrium position of the particle. According to Eq. (15), we can arbitrarily change the slip length by changing the coefficient r of the slip boundary condition to control the equilibrium position of the particle. In this way, we present a scheme to actively control the particle position in inertial microfluidics. The motion of particles can be controlled without the external force or the channel with special geometry.

Figure 5 depicts the scheme to actively control of particle equilibrium positions by using the slip boundary condition at the upper boundary in Poiseuille flow. Our simulations are carried out in a two–dimensional rectangular domain 1000×100 (lattice units). The corresponding macroscopic width of the channel is 20 μm. The fluid density is 1×10^3 kg/m^3 and the kinematic viscosity coefficient is $\upsilon = 1 \times 10^{-6}$m^2/s, the density of particles is equal to the fluid. Reynolds number (Re) is a dimensionless number to characterize fluid flow and is expressed as $\mathrm{Re} = HU/\upsilon$, where U is the mean fluid velocity in Poiseuille flow without a particle. The pressure boundary condition is applied at the inlet and outlet of the channel. To demonstrate the effect of active control, three kinds of particles with different shapes are applied in the following simulations. In the beginning, the particles migrate in the microchannel without the boundary slip and reach to their equilibrium positions. At 0.5 ms, some slip lengths are applied to the upper boundary of the microchannel, and the particles shift to new equilibrium positions quickly. Finally, they are pushed into different branches.

A. Circular particle

At first, we investigate to manipulate the circular particle, and the diameters are 4 and 6 μm. The migration trajectories, horizontal velocity, and period time of the circular particles when the slip length is 0, 2, 6, 10, 14, and 18 μm are shown in Fig. 8. The Reynolds number of Poiseuille flow is 24 when the slip length is 0 μm. The migration trajectories of the circular particle with the a diameter of 6 μm are shown in Fig. 6(a). The straight black line is the migration trajectory when the upper channel is no-slip, namely the classical Segré-Silberberg effect. The process from placing the particles to reaching the equilibrium position in the first half of the channel is omitted. With the increase of the slip length, the velocity distribution of the flow field will change. The circular particles will gradually migrate upward and reach to the equilibrium position.

Figure 6(b) shows the vertical equilibrium positions and rotating periods of circular particles changing with slip lengths. When the slip length increase from 0 to 18 μm, the equilibrium positions

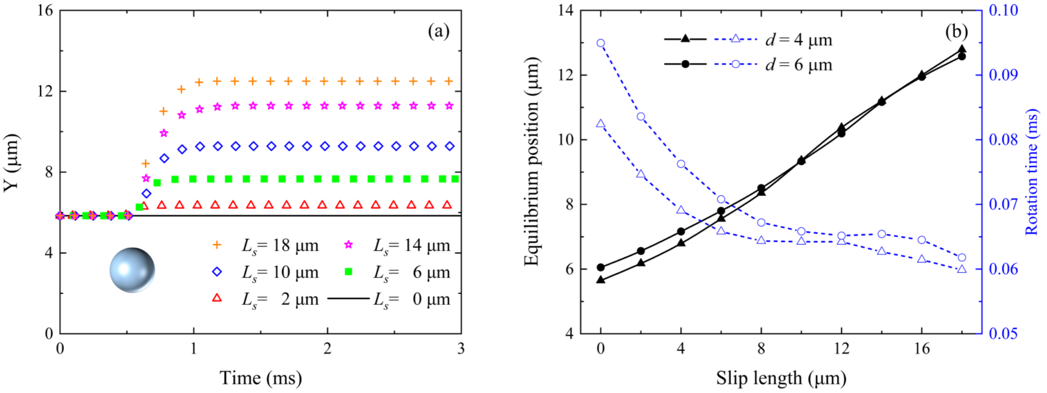

FIG. 6. The migrations and equilibriums of circular particles in the channel flows with various unilateral slip lengths. (a) The migration trajectories and (b) the vertical equilibrium positions and the rotating periods of the circular particles, where d is the diameter of the circular particle.

of the circular particles increase linearly and gradually move toward the upper boundary. On the contrary, the rotation time becomes shorter. The maximum period time of the circular particle is only 0.096 ms. However, when the slip length is 10–14 μm, the period time of the circular particle becomes basically the same. It is obvious that the larger particle, the longer the rotating period time is. The size of the particle has little influence on the vertical equilibrium position.

B. Elliptical particle

Then, the manipulations of two kinds of elliptical particles are simulated. The long axis of the elliptical particle is fixed at 6 μm, while the short axes are 2 and 3 μm. As shown in Fig. 7(a), due to the noncircular geometry of elliptical particles and the parabolic velocity distribution in the channel, the motions of the elliptical particles are accompanied by complex rotation and oscillations. Similar to circular particles, elliptical particles will reach different equilibrium positions with different slip lengths. Here, the equilibrium position is defined as the average position in a rotation period after the particle is in equilibrium.

The vertical equilibrium positions and the rotating periods changing with the slip length of elliptical particles are shown in Fig. 7(b). The influence of slip length on the vertical equilibrium

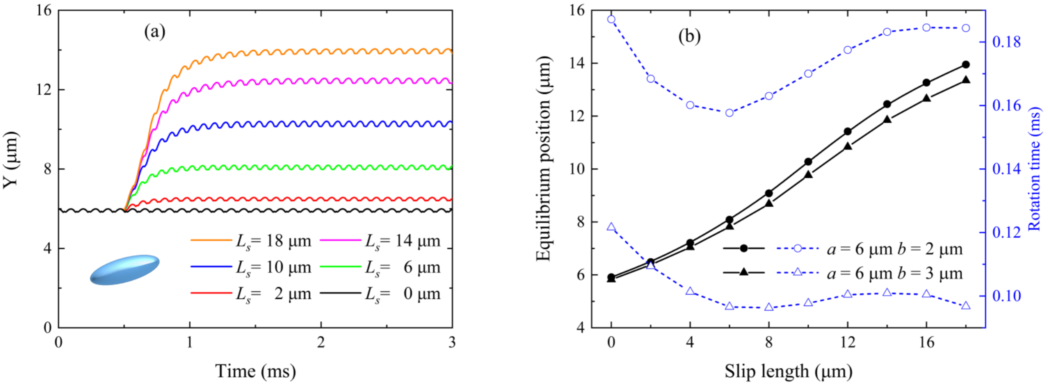

FIG. 7. The migrations and equilibriums of elliptical particles in the channel flows with various unilateral slip lengths. (a) The migration trajectories and (b) the vertical equilibrium positions and the rotating periods of the elliptical particles, where a and b are the long axis and short axis of the elliptical particle.

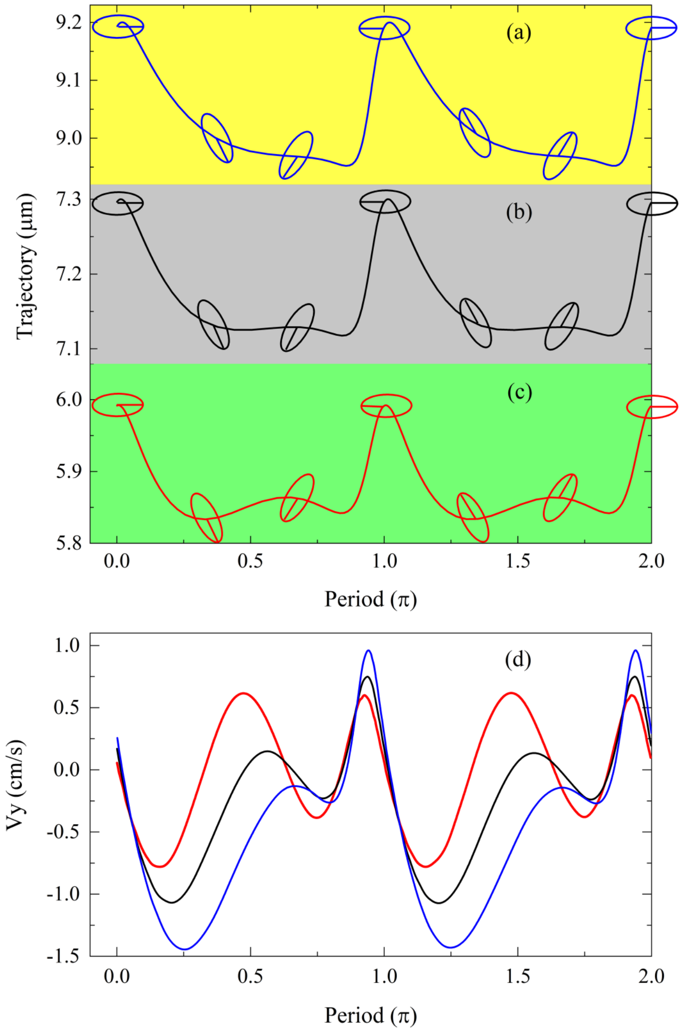

FIG. 8. The migration trajectory and angular orientation of the elliptical particle with slip lengths of (a) 8 μm, (b) 4 μm, (c) 0 μm, and (d) the vertical velocities of the elliptical particles with slip lengths of 0 (red line), 4 (black line), and 8 μm (blue line).

positions and period time of elliptical particles is similar to that of circular particles. The influence of the size and aspect ratio of particles on equilibrium positions is not distinct. However, it is very clear that the particle with the larger aspect ratio has a shorter rotation period and rotates faster. Because of the noncircular geometry, the area of thrust surface of the elliptical particle is uneven in the flow field. So, the same hydraulic force pushes the flatter elliptical particle to rotate more slowly. This is consistent with the observations in the related study [29]. The period times of the elliptical particle with different slip lengths are all greater than 0.096 ms and the maximum reaches 0.188 ms. The similar rotational periods of ellipsoid particles were reported in the experiments and simulations by Masaeli *et al.* [51]. Obviously, the rotations of elliptical are slower than circular particles, bacause their noncircular geometries result in more resistance in the rotational process.

Figures 8(a)–8(c) depict the trajectories and angular orientation of the elliptical particle with the slip length of 8, 4, and 0 μm, together with the orientations of the elliptical particle in various typical positions. Here, the clockwise is defined as the positive direction to investigate the rotation

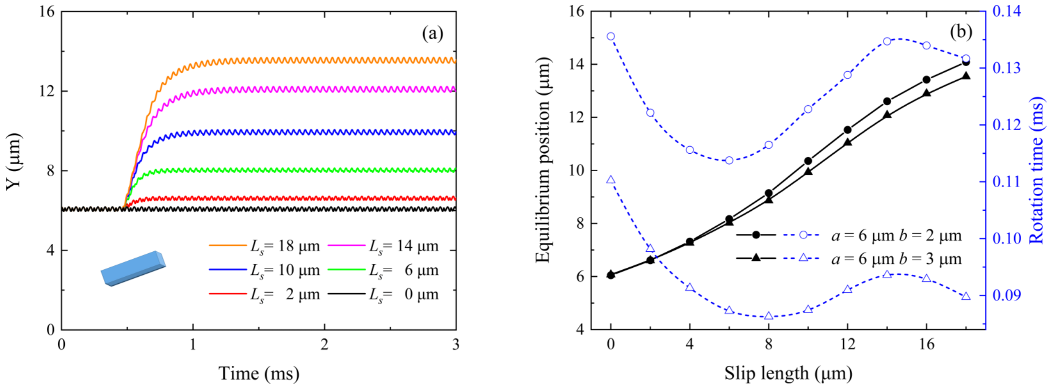

FIG. 9. The migrations and equilibriums of rectangular particles in the channel flows with various unilateral slip lengths. (a) The migration trajectories and (b) the vertical equilibrium positions and the rotating periods of the rectangular particles, where *a* and *b* are the length and width of the rectangle.

of the particle. The steering angles are 0, $1/3\pi$, $2/3\pi$, π, $4/3\pi$, $5/3\pi$, and 2π, respectively. The migration trajectory of the elliptical particle is like a saddle. The saddle shape can be considered as the combined action of the hydrodynamic force, the wall effect and the periodic oscillation. In steady state, the lateral migration amplitude of elliptic particles inside a rotation period is 0.16 μm at $L_s = 0$ μm. As the slip length increases to 8 μm, the lateral migration amplitude increases to 0.24 μm. It indicates that the lateral migration amplitude of elliptic particles inside a rotation period increases significantly with the increase of the slip length. When the slip length is 0 μm, the fluctuation amplitude of the elliptical particle has a small wave peak during the steering angle 0.25–0.75π in the half rotation period. However, the small wave peak gradually disappears as the slip length increases from 0 to 8 μm. So, the oscillation trajectories of the particles will also change accordingly with the increase of the slip length.

Figure 8(d) shows vertical velocities of the elliptical particle with different slip lengths. The patterns of the vertical velocities of ellipses with different slip lengths are similar within a single period. It suggests that the elliptical particles with the same aspect ratio have similar migration trajectories at different slip lengths. When the period is 0.25–0.5π and 1.25–1.75π, the vertical velocity gradually changes from negative to positive. However, the vertical velocity remains negative in this interval when the slip length is greater than 0 μm, because the boundary slip causes the velocity of the flow field and the rotation speed of the particle to increase so that the particle completes a quarter of the cycle before the vertical velocity becomes positive. This confirms that the small wave peak disappears as the slip length increases gradually in Figs. 8(a) and 8(b). Observing the vertical velocities of the particle in the fluctuating process, it can be found that the elliptical particle migrates with a large cross–stream velocity in the vertical direction if the slip length is large enough. These indicate that the oscillation amplitude of the elliptical particle with a long slip length is also more obvious than the shorter one.

C. Rectangular particle

Next, the motions of rectangular particles with the size of 6 × 3 μm and 6 × 2 μm at different slip lengths are numerically investigated. Figure 9(a) shows that the trajectories have similar oscillation amplitudes as the elliptical particle. The migration trajectories of the rectangle ones are quite similar to the classical Segré-Silberberg effect, although their unsymmetrical geometries cause additional fluctuations and nonuniform rotation in the process of migration. Similarly, the rectangular particle will reach different equilibrium positions with different slip lengths.

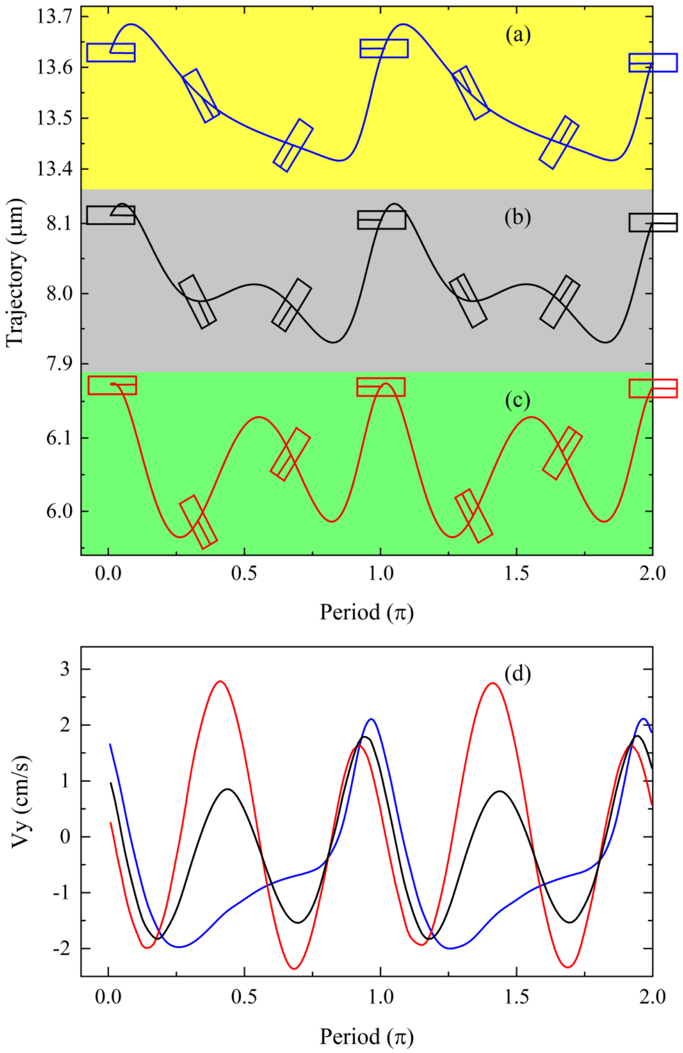

FIG. 10. The migration trajectory and angular orientation of the rectangular particle with slip lengths of (a) 18 μm, (b) 6 μm, (c) 0 μm, and (d) the vertical velocities of the rectangular particles with slip lengths of 0 (red line), 6 (black line), and 18 μm (blue line).

Figure 9(b) shows that with the increase of the slip length, the vertical equilibrium positions also gradually move toward the upper channel wall. This is in agreement with the previous studies on the lateral migrations of circular or elliptical particles. Both the elliptical and rectangular particles have the noncircular geometry, the relation between the rotation period and aspect ratio of the rectangular particle is the same as that of the ellipse.

Figure 10 shows the steering angle, vertical trajectory, and vertical velocities of the rectangular particles with slip lengths of 0, 6, and 18 μm, together with the orientations of the rectangular particle in various typical positions. With the increase of the slip length, the oscillation of the rectangular particle gradually changes from three wave peaks to one. When the slip length is 0 μm and the steering angle is $0\text{–}0.27\pi$ in half a rotation period, the alternating force caused by the rotation of the rectangular particles acts as a sinking force to make the particles move downward. However, the alternating force becomes an ascending force when the steering angle is

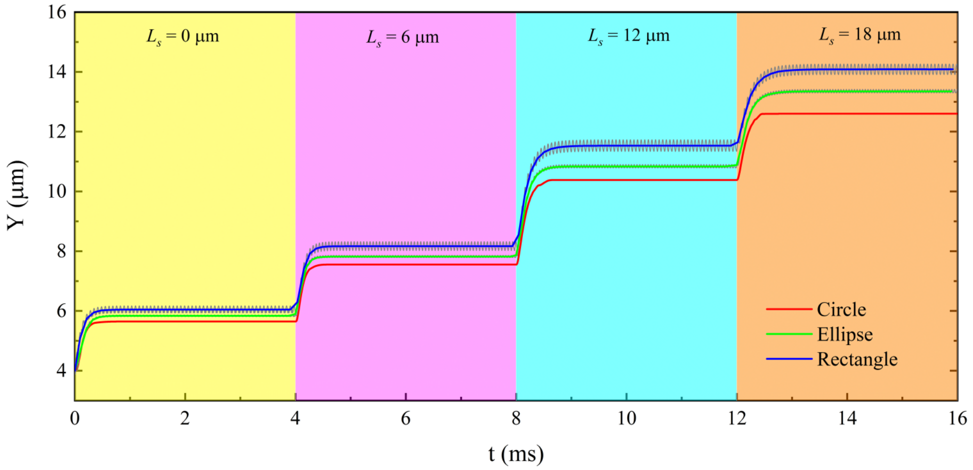

FIG. 11. Active control of the particulate equilibrium positions by continuously adjusting the boundary slip in real time. The red, green, and blue line represents the circular, elliptical, and rectangular particle, respectively. L_s is the real-time slip length of the upper boundary.

$0.27–0.54\pi$. In the same way, while the steering angle is $0.54–0.82\pi$ and $0.82–1\pi$, the alternating force makes the particle go through the ups and downs again. In the angular range of $0.27–0.82\pi$ and $1.27–1.82\pi$, the oscillation of the particle can be seen clearly without the slip length. When the slip length is 6 μm, the small wave peak is not obvious. When the slip length increases to 18 μm, the small wave peak disappears completely. These prove that the oscillation of the rectangular particle changes with the increase of the slip length.

The vertical velocities of the rectangular particle with different slip lengths are shown in Fig. 10(d). Ignoring the differences in rotation periods, the patterns of vetical velocities are different within a single period. It suggests that the rectangular particles have different vertical motions at different slip lengths. When the steering angle is $0.27–0.82\pi$ or $1.27–1.82\pi$, the negative vertical velocity first increases to positive and then decreases to negative when the slip length is 0 μm. The oscillation of rectangular particle is obvious during this period if the slip length is small. However, the boundary slip causes the acceleration of the velocity of the flow field and results in the shortening of the particle rotation period. The negative vertical velocity cannot increase to positive with the increase of the slip length in this angular range, resulting in insignificant particle fluctuation.

D. Active control in real time

Finally, the active controls of vertical particle positions in real time are illustrated by successive adjustments of the slip length of the upper boundary. Three shapes of particles are simulated. The diameter of the circular particle is 4 μm, the long and short axes of the ellipse particle are 6 and 3 μm, and the length and width of the rectangle particle are 6 and 2 μm, respectively. Figure 11 draws the real-time trajectories of these particles. The green and blue lines represent the average positions of the two kinds particles in each rotation period. With the increase of the slip length from 0 to 18 μm, the vertical positions of the particles are immediately shifted toward the upper boundary. The particles will eventually migrate to different equilibrium positions, and the rectangular particle results in the largest oscillations and is the closest to the upper boundary. Because of the noncircular geometry of the elliptical and rectangular particles, their motions are accompanied by uneven rotation and regular oscillations, as shown by the grey lines in Fig. 11. It is clear that after the slip length is changed, all the particles can reach to the new equilibrium positions in only 1 μs.

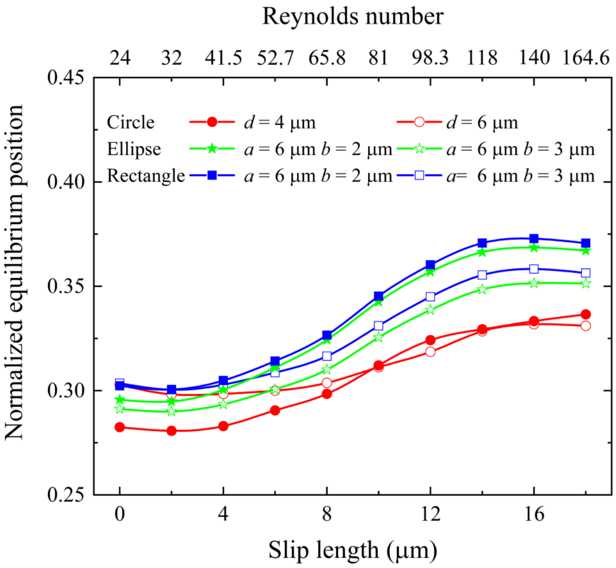

FIG. 12. The normalized equilibrium positions of particles in the channel widened by the relevant slip length. The red, green, and blue lines represent the circular, elliptical, and rectangular particles, respectively.

In Figs. 6(b), 7(b), and 9(b), we found that the rotating periods of particles did not decrease linearly with the increase of the slip length. Considering the parabolic velocity distribution of Poiseuille flow, there are significant differences in velocity among stream layers. Figure 12 shows that with the increase of the slip length, the particles' normalized equilibrium positions gradually move from 0.3 to 0.35. The normalized equilibrium position is the dimensionless equilibrium position of the particle in the channel widened by the relevant slip length. That is, with the increase of the Reynolds number, the normalized equilibrium position gradually moves upwards. When the slip length is less than 40 μm, the normalized equilibrium position is maintained at about 0.3. The particle is close to the wall, and the difference in the velocity between the upper and lower stream layers around the particle is large. Thus, the rotation period of particles reduces in this interval. When the slip length increases from 8 to 14 μm, the normalized equilibrium position increase to 0.35. The particle gradually moves away from the wall, and the difference in velocity between the upper and lower stream layer around the particle decreases. This causes the rotation period of the particle becomes longer. So, it is clearly shown in Figs. 6(b), 7(b), and 9(b) that the rotation periods of three particles increase gradually when the slip length increases from 8 to 14 μm.

V. CONCLUSION

In this paper, we utilize the boundary slip effect to regulate the velocity distribution of fluid in the microchannel and present a scheme to actively control the particle position in inertial microfluidics. A series of numerical simulations of different shape particles migrating laterally in Poiseuille flow with BSR slip boundary condition are performed by the lattice Boltzmann method with single relaxation time. The hydrodynamic force is evaluated by the Galilean-invariant momentum exchange method. The flow field of a microchannel with a unilateral slip boundary is equivalent to that of the microchannel widened by the relevant slip length, and the particle equilibrium positions in the two microchannels are consistent consequently. The effectivity and feasibility of the model are verified by three kinds of particles, namely circular, elliptical, and rectangular. In addition, because the elliptical and rectangular particles have noncircular geometry, their motions are accompanied by uneven rotation and regular vibration. The flow field and the particle motion are affected by the slip boundary conditions. When the slip boundary condition is used, the change of velocity distribution of the flow field results in accelerating the speed of particles' rotation and shortening the rotation period. It can be found that the fluctuation amplitude of the noncircular particles will increase as the slip length gradually increases. Under the slip boundary condition, some original fluctuations caused by the rotation of the particles will also disappear.

With a greater simulation of the boundary slip at 2D steady Poiseuille flow to the active control of the particulate equilibrium positions, we will be able to extend this scheme to 3D situations, and the section shape of the microchannel will be investigated in detail. Ultimately, in practical applications, we would like to be able to prepare surfaces on which the interfacial flow can be altered, perhaps by varying the shear rate of the liquid or by tuning other parameters of the surface, such as surface charge. Electrowetting could be an effective way to adjust the boundary slip. Many studies reported that electrowetting could change the surface wettability, namely the contact angle, and the wettability tuned from hydrophilic to hydrophobic influences the boundary slip strongly [45,52–54]. The engineering of such surfaces will be of great interest in a number of applications and a range of technologies to promote the active manipulation of particles in microfluidics and realize more accurate and flexible focusing, separating, and transport.

ACKNOWLEDGMENTS

This work was supported by the National Natural Science Foundation of China (Grants No. 11862003, No. 81860635, and No. 12062005), the Project of Guangxi Natural Science Foundation (Grants No. 2017GXNSFDA198038 and No. 2018JJA110023), Guangxi "Bagui Scholar" Teams for Innovation and Research Project, Guangxi Collaborative Innovation Center of Multisource Information Integration and Intelligent Processing.

APPENDIX A: MOVING BOUNDARY CONDITIONS

The LBM has also been effectively applied to simulations of particulate suspensions in fluids. The curved boundaries of the particles are usually approximated by a zigzag staircase thus bounce-back boundary condition can be directly applied. Filippova and Hanel [55] proposed a curve boundary condition in 1998. Their method constructed a fictitious equilibrium distribution function for nonfluid nodes, so as to find the missing distribution function for fluid nodes on the boundary. Mei *et al.* [56] developed a second-order accurate treatment of the boundary condition for a curved boundary, which is an improvement of a scheme of Filippova and Hanel. Despite the success of these methods in the curved boundaries, there is no rigorous theory on the treatment of moving boundaries. Lallemand and Luo [57,58] proposed the quadratic interpolation method to treat the curved boundary and the moving particular boundary. Here, their method is adopted to treat the moving boundary of particles in the fluid.

A schematic diagram of the curved fluid-solid boundary condition is shown in Fig. 13. The parameter q defines the fraction in the fluid region of a grid spacing intersected by the boundary. The node $\boldsymbol{x}_s$ is the boundary node and $\boldsymbol{x}_w$ is the intersection point on the fluid-solid link. To avoid extrapolations, the scheme is divided into two parts according to the value of q. After collision and advection, the interpolation formulas are described as

$$\begin{cases} f_{\bar{i}}(\boldsymbol{x}_1,t) = q(1+2q)\tilde{f}_i(\boldsymbol{x}_1,t) + (1-4q^2)\tilde{f}_i(\boldsymbol{x}_2,t) - q(1-2q)\tilde{f}_i(\boldsymbol{x}_3,t) + 3\omega_i(\boldsymbol{e}_i\cdot\boldsymbol{u}_w) & q \leqslant 1/2 \\ f_{\bar{i}}(\boldsymbol{x}_1,t) = \frac{1}{q(1+2q)}\tilde{f}_i(\boldsymbol{x}_1,t) + \frac{2q-1}{q}f_{\bar{i}}(\boldsymbol{x}_2,t) - \frac{2q-1}{2q+1}f_{\bar{i}}(\boldsymbol{x}_3,t) + \frac{3\omega_i}{q(2q+1)}(\boldsymbol{e}_i\cdot\boldsymbol{u}_w) & q > 1/2 \end{cases}, \tag{A1}$$

where $\tilde{f}_i(\boldsymbol{x},t)$ is the distribution function streamed from $\boldsymbol{x}$ in the i direction. $\boldsymbol{x}_2$ and $\boldsymbol{x}_3$ are two points adjacent to $\boldsymbol{x}_1$ along the i direction for interpolation, $\boldsymbol{u}_w$ represents the velocity of the moving boundary at the point of the intersection $\boldsymbol{x}_w$, and ω_i takes $2/9$ for $i = 1, 2, 3, 4$ and $1/18$ for

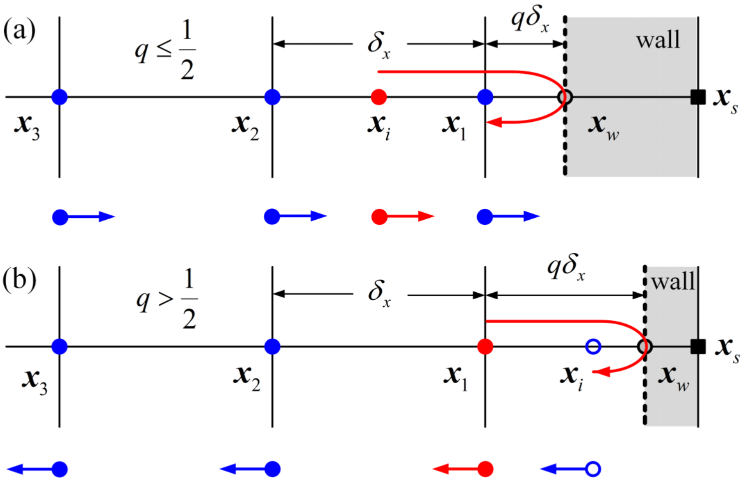

FIG. 13. Schematic diagram of curved fluid-solid boundary condition. (a) $q \leqslant 1/2$ and (b) $q > 1/2$, where $q = (\boldsymbol{x}_1 - \boldsymbol{x}_w)/(\boldsymbol{x}_1 - \boldsymbol{x}_s)$.

$i = 5, 6, 7, 8$ [59]. When $q \leqslant 1/2$, the interpolation calculation is performed before flow and rebound. When $q > 1/2$, interpolation calculation is performed after flow and rebound.

APPENDIX B: HYDRODYNAMIC FORCE EVALUATION

The hydrodynamic force in the lattice Boltzmann method can be efficiently evaluated by using a momentum exchange method. Ladd *et al.* [60] proposed the original momentum exchange method, which lays the particle boundary discretely and approximately at the middle of the link between a solid node and a fluid node, namely a fluid-solid link. A momentum item based on the boundary velocity was added to the distribution functions which were bounced back from the particle boundary, and the momentum-exchange occurred during the streaming step. Aidun *et al.* [61] improved Ladd's model by directly representing the solid particle without fluid inside. The momenta of the covered and uncovered nodes were involved in the force evaluation for moving solid particles. However, their effect was not investigated in detail. A common drawback in Ladd's and Aidun's method is that the boundary geometry, which is located at the middle of fluid-solid links, is zigzag. Mei *et al.* [62] introduced the curved boundary conditions in the momentum–exchange method so that the particulate geometry could be accurately represented on the grid level.

As shown in Fig. 14, a moving boundary is located between a fluid node $\boldsymbol{x}_f$ and a boundary node $\boldsymbol{x}_s$. The boundary has a vector velocity $\boldsymbol{v}$ at the point of intersection $\boldsymbol{w}$. Wen *et al.* [33,34] introduced the relative velocity into the interfacial momentum transfer to compute the hydrodynamic force and

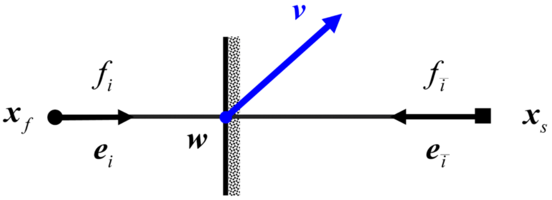

FIG. 14. Schematic diagram to illustrate a moving boundary crossing a fluid-solid link at the point of intersection $\boldsymbol{w}$. $\boldsymbol{x}_f$ and $\boldsymbol{x}_s$ denote the adjacent fluid and boundary nodes. The boundary has a velocity $\boldsymbol{v}$ at the point $\boldsymbol{w}$.

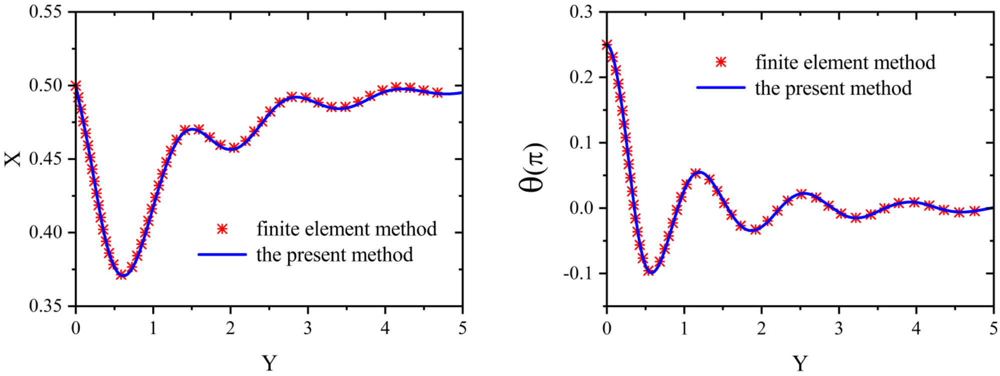

FIG. 15. Trajectories and orientations of elliptical cylinder sedimentations with the parameters $\alpha = 0.5$ and $\beta = 0.25$. X and Y are the positions normalized to the pipe width and length, respectively.

proposed a Galilean invariant momentum (GME) exchange equation:

$$\boldsymbol{F}(\boldsymbol{x}_s) = (\boldsymbol{e}_i - \boldsymbol{v})f_i(\boldsymbol{x}_f, t) - (\boldsymbol{e}_{\bar{i}} - \boldsymbol{v})f_{\bar{i}}(\boldsymbol{x}_s, t). \tag{B1}$$

Especially, the algorithm meets full Galilean invariance and is independent of boundary geometries. The total hydrodynamic force and torque are calculated by

$$\boldsymbol{F} = \sum \boldsymbol{F}(\boldsymbol{x}_w) \tag{B2}$$

and

$$\boldsymbol{T} = \sum (\boldsymbol{x}_w - \boldsymbol{R}) \times \boldsymbol{F}(\boldsymbol{x}_w), \tag{B3}$$

where $\boldsymbol{F}$ and $\boldsymbol{T}$ are the summation of force and torque on each $\boldsymbol{x}_w$, and $\boldsymbol{R}$ is the mass center of the solid particle. GME is simple, efficient in computation, and clearly expressed physically. Previous studies have shown that GME can greatly improve the computational accuracy and robustness of moving boundaries in the dynamic fluid [33].

APPENDIX C: VALIDATION OF THE NUMERICAL METHOD

To verify the numerical method, the simulations of 2D ellipse sedimentation in a vertical channel and 3D particle migration in Poiseuille flow were performed.

In the simulations of ellipse sedimentation, an inclined elliptical particle is released on the centerline of the channel. Since the mass density of the ellipse is slightly greater than that of the fluid, the particle descends, rotates and translates under the gravitational force and the hydrodynamic force. The major and minor axes of the ellipse are a and b, and the width of the channel is L. The aspect ratio and blockage ratio are defined by $\alpha = b/a$ and $\beta = a/L$, respectively. The fluid density is 1 $\mathrm{mg/mm^3}$, while the density of the elliptical particle is 1.1 $\mathrm{mg/mm^3}$.

In the first case, the width of the channel takes 120 lattice units, and the corresponding macroscopic width is 4 mm. The aspect ratio is $\alpha = 0.5$ and the blockage ratio is $\beta = 0.25$. The particle is released at the middle of the channel with an initial angle of $\theta = \pi/4$ to the horizontal axis. The trajectories and the angle of obliquity of an elliptical cylinder sedimentation are shown in Fig. 15. The particle moves to the left and rotates clockwise till a negative angle of obliquity. Eventually, the particle settles on the centerline of the channel and takes a horizontal posture. The second case has a sizable blockage ratio $\beta = 13/22$ and the width of the channel is 132 lattice units. The aspect ratio remains the same as in the first case. Figure 16 shows the trajectories and orientations of an elliptical cylinder sedimentation when the elliptical particle is released at the middle of the channel in the horizontal direction with the initial angle $\theta = \pi/3$. The equilibrium state of the elliptical particle

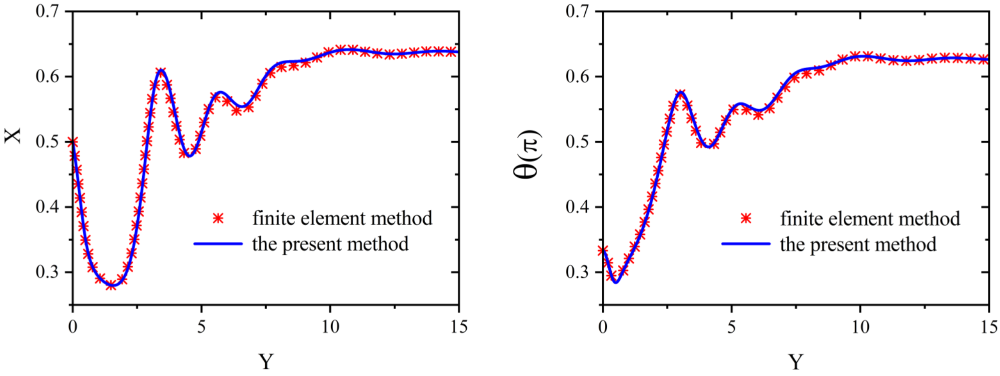

FIG. 16. Trajectories and orientations of elliptical cylinder sedimentations with the parameters $\alpha = 0.5$ and $\beta = 13/22$. X and Y are the positions normalized to the pipe width and length, respectively.

deviates from the centerline of the channel and keeps a nonzero angle of obliquity. The present simulations are in excellent agreement with the results from the finite element method [63,64].

The numerical method is further verified by comparing with the experiment, in which Karnis *et al.* studied the migrations of a neutrally buoyant sphere in Poiseuille flow, namely the Segré-Silberberg effect. The radii of the tube and the sphere are $R = 0.2$ cm and $r = 0.061$ cm, respectively. The density of the fluid and sphere is 1.05 g/cm^3. The corresponding radius of the sphere is 9.5 lattice units and Reynold number is 0.198. The pressure boundary condition is applied at the inlet and outlet of the channel. The particles are released at $Y = 0.21$ and $Y = 0.68$, respectively, where Y is the dimensionless radial position r^*/R, and r^* is the distance to the centerline of the tube. The migration trajectories of spheres are shown in Fig. 17. The numerical results are in excellent agreement with those of the experiments [65].

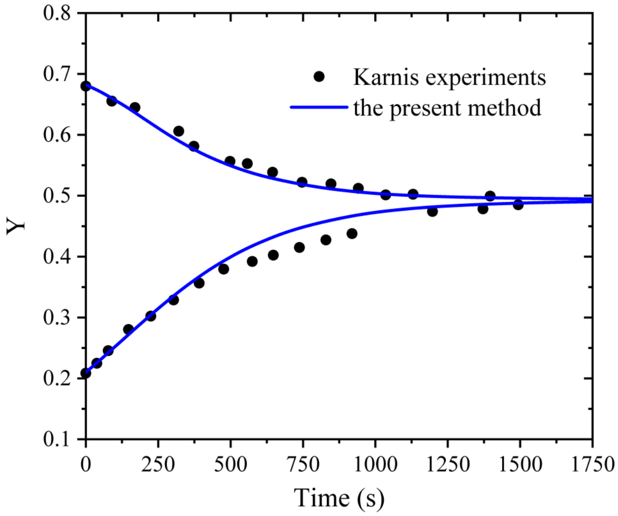

FIG. 17. Migration trajectories of a neutrally buoyant sphere in Poiseuille flow. Y is the dimensionless radial position of the tube.

[1] D. Di Carlo, Inertial microfluidics, Lab Chip **9**, 3038 (2009).
[2] G. M. Whitesides, The origins and the future of microfluidics, Nature (London) **442**, 368 (2006).
[3] T. M. Squires and S. R. Quake, Microfluidics: Fluid physics at the nanoliter scale, Rev. Mod. Phys. **77**, 977 (2005).
[4] Q. Zhao, D. Yuan, J. Zhang, and W. Li, A review of secondary flow in inertial microfluidics, Micromachines **11**, 461 (2020).
[5] W. Tang, S. Zhu, D. Jiang, L. Zhu, J. Yang, and N. Xiang, Channel innovations for inertial microfluidics, Lab Chip **20**, 3485 (2020).
[6] S. Razavi Bazaz, A. Mashhadian, A. Ehsani, S. C. Saha, T. Krüger, and M. Ebrahimi Warkiani, Computational inertial microfluidics: A review, Lab Chip **20**, 1023 (2020).
[7] A. Mashhadian and A. Shamloo, Inertial microfluidics: A method for fast prediction of focusing pattern of particles in the cross section of the channel, Anal. Chim. Acta **1083**, 137 (2019).
[8] P. Paiè, F. Bragheri, D. Di Carlo, and R. Osellame, Particle focusing by 3D inertial microfluidics, Microsyst. Nanoeng. **3**, 17027 (2017).
[9] M. S. Syed, M. Rafeie, D. Vandamme, M. Asadnia, R. Henderson, R. A. Taylor, and M. E. Warkiani, Selective separation of microalgae cells using inertial microfluidics, Bioresour. Technol. **252**, 91 (2018).
[10] J. P. Dijkshoorn, M. A. Schutyser, R. M. Wagterveld, C. G. Schroën, and R. M. Boom, A comparison of microfiltration and inertia-based microfluidics for large-scale suspension separation, Sep. Purif. Technol. **173**, 86 (2017).
[11] G. Segré and A. Silberberg, Radial particle displacements in Poiseuille flow of suspensions, Nature (London) **189**, 209 (1961).
[12] D. Di Carlo, D. Irimia, R. G. Tompkins, and M. Toner, Continuous inertial focusing, ordering, and separation of particles in microchannels, Proc. Nat. Acad. Sci USA **104**, 18892 (2007).
[13] H. Ramachandraiah, S. Ardabili, A. M. Faridi, J. Gantelius, J. M. Kowalewski, G. Mårtensson, and A. Russom, Dean flow-coupled inertial focusing in curved channels, Biomicrofluidics **8**, 034117 (2014).
[14] A. A. S. Bhagat, S. S. Kuntaegowdanahalli, N. Kaval, C. J. Seliskar, and I. Papautsky, Inertial microfluidics for sheath-less high-throughput flow cytometry, Biomed. Microdevices **12**, 187 (2010).
[15] J. Sun, M. Li, C. Liu, Y. Zhang, D. Liu, W. Liu, G. Hu, and X. Jiang, Double spiral microchannel for label-free tumor cell separation and enrichment, Lab Chip **12**, 3952 (2012).
[16] J. Zhang, W. Li, M. Li, G. Alici, and N. T. Nguyen, Particle inertial focusing and its mechanism in a serpentine microchannel, Microfluid. Nanofluid. **17**, 305 (2014).
[17] A. T. Ciftlik, M. Ettori, and M. A. Gijs, High throughput-per-footprint inertial focusing, Small **9**, 2764 (2013).
[18] M. A. Samaha, H. Vahedi Tafreshi, and M. Gad-el Hak, Modeling drag reduction and meniscus stability of superhydrophobic surfaces composed of random roughness, Phys. Fluids **23**, 012001 (2011).
[19] C. L. Navier, Memorie sur les lois du lois du mouvement des fluides, Mem. Acad. Sci. Inst. Fr. **6**, 298 (1823).
[20] B. Y. Cao, J. Sun, M. Chen, and Z. Y. Guo, Molecular momentum transport at fluid-solid interfaces in MEMS/NEMS: A review, Int. J. Mol. Sci. **10**, 4638 (2009).
[21] D. Li, D. Jing, Y. Pan, B. Bhushan, and X. Zhao, Study of the relationship between boundary slip and nanobubbles on a smooth hydrophobic surface, Langmuir **32**, 11287 (2016).
[22] A. Minakov, V. Rudyak, A. Dekterev, and A. Gavrilov, Investigation of slip boundary conditions in the T-shaped microchannel, Int. J. Heat Fluid Flow **43**, 161 (2013).
[23] D. Schäffel, K. Koynov, D. Vollmer, H. J. Butt, and C. Schönecker, Local Flow Field and Slip Length of Superhydrophobic Surfaces, Phys. Rev. Lett. **116**, 134501 (2016).
[24] C. Lee, C. H. Choi, and Chang-Jin Kim, Structured Surfaces for a Giant Liquid Slip, Phys. Rev. Lett. **101**, 064501 (2008).
[25] C. Lee and C. J. Kim, Maximizing the giant liquid slip on superhydrophobic microstructures by nanostructuring their sidewalls, Langmuir **25**, 12812 (2009).
[26] S. Ansumali and I. V. Karlin, Single relaxation time model for entropic lattice Boltzmann methods, Phys. Rev. E **65**, 056312 (2002).

[27] D. K. Sun, Y. Wang, A. P. Dong, and B. D. Sun, A three-dimensional quantitative study on the hydrodynamic focusing of particles with the immersed boundary—Lattice Boltzmann method, Int. J. Heat Mass Transfer **94**, 306 (2016).

[28] H. Huang, X. Yang, M. Krafczyk, and X. Y. Lu, Rotation of spheroidal particles in Couette flows, J. Fluid Mech. **692**, 369 (2012).

[29] B. Wen, H. Chen, Z. Qin, B. He, and C. Zhang, Lateral migration and nonuniform rotation of suspended ellipse in Poiseuille flow, Comput. Math. Appl. **78**, 1142 (2019).

[30] B. H. Wen, Y. Y. Chen, R. L. Zhang, C. Y. Zhang, and H. P. Fang, Lateral migration and nonuniform rotation of biconcave particle suspended in Poiseuille flow, Chin. Phys. Lett. **30**, 64701 (2013).

[31] C. Liu, C. Xue, J. Sun, and G. Hu, A generalized formula for inertial lift on a sphere in microchannels, Lab Chip **16**, 884 (2016).

[32] H. Liu and Y. Zhang, Modelling thermocapillary migration of a microfluidic droplet on a solid surface, J. Comput. Phys. **280**, 37 (2015).

[33] B. Wen, C. Zhang, Y. Tu, C. Wang, and H. Fang, Galilean invariant fluid-solid interfacial dynamics in lattice Boltzmann simulations, J. Comput. Phys. **266**, 161 (2014).

[34] B. Wen, C. Zhang, and H. Fang, Hydrodynamic force evaluation by momentum exchange method in lattice Boltzmann simulations, Entropy **17**, 8240 (2015).

[35] S. Chen and G. D. Doolen, Lattice Boltzmann method for fluid flows, Annu. Rev. Fluid Mech. **30**, 329 (1998).

[36] A. G. Xu, G. C. Zhang, Y. B. Gan, F. Chen, and X. J. Yu, Lattice Boltzmann modeling and simulation of compressible flows, Front. Phys. **7**, 582 (2012).

[37] F. Bösch and I. V. Karlin, Exact Lattice Boltzmann Equation, Phys. Rev. Lett. **111**, 090601 (2013).

[38] A. Mazloomi M, S. S. Chikatamarla, and I. V. Karlin, Entropic Lattice Boltzmann Method for Multiphase Flows, Phys. Rev. Lett. **114**, 174502 (2015).

[39] P. Lallemand and L. S. Luo, Theory of the lattice Boltzmann method: Acoustic and thermal properties in two and three dimensions, Phys. Rev. E **68**, 036706 (2003).

[40] C. Neto, D. R. Evans, E. Bonaccurso, H. J. Butt, and V. S. Craig, Boundary slip in Newtonian liquids: A review of experimental studies, Rep. Prog. Phys. **68**, 2859 (2005).

[41] N. V. Churaev, V. D. Sobolev, and A. N. Somov, Slippage of liquids over lyophobic solid surfaces, J. Colloid Int. Sci. **97**, 574 (1984).

[42] B. V. Paranjape, Friction at the solid interface in a fluid flow, Phys. Lett. A **137**, 285 (1989).

[43] R. Pit, H. Hervet, and L. Léger, Direct Experimental Evidence of Slip in Hexadecane: Solid Interfaces, Phys. Rev. Lett. **85**, 980 (2000).

[44] V. S. J. Craig, C. Neto, and D. R. M. Williams, Shear-Dependent Boundary Slip in an Aqueous Newtonian Liquid, Phys. Rev. Lett. **87**, 054504 (2001).

[45] Y. Zhu and S. Granick, Rate-Dependent Slip of Newtonian Liquid at Smooth Surfaces, Phys. Rev. Lett. **87**, 096105 (2001).

[46] S. Succi, Mesoscopic Modeling of Slip Motion at Fluid-Solid Interfaces with Heterogeneous Catalysis, Phys. Rev. Lett. **89**, 064502 (2002).

[47] Z. Guo and C. Zheng, Analysis of lattice Boltzmann equation for microscale gas flows: Relaxation times, boundary conditions and the Knudsen layer, Int. J. Comput. Fluid Dyn. **22**, 465 (2008).

[48] Z. Chai, Z. Guo, L. Zheng, and B. Shi, Lattice Boltzmann simulation of surface roughness effect on gaseous flow in a microchannel, J. Appl. Phys. **104**, 014902 (2008).

[49] C.-H. Choi and C.-J. Kim, Large Slip of Aqueous Liquid Flow Over a Nanoengineered Superhydrophobic Surface, Phys. Rev. Lett. **96**, 066001 (2006).

[50] J. Ou, B. Perot, and J. P. Rothstein, Laminar drag reduction in microchannels using ultrahydrophobic surfaces, Phys. Fluids **16**, 4635 (2004).

[51] M. Masaeli, E. Sollier, H. Amini, W. Mao, K. Camacho, N. Doshi, S. Mitragotri, A. Alexeev, and D. Di Carlo, Continuous Inertial Focusing and Separation of Particles by Shape, Phys. Rev. X **2**, 031017 (2012).

[52] F. Mugele and J. C. Baret, Electrowetting: From basics to applications, J. Phys.: Condens. Matter **17**, R705 (2005).

[53] P. Teng, D. Tian, H. Fu, and S. Wang, Recent progress of electrowetting for droplet manipulation: From wetting to superwetting systems, Mater. Chem. Front. **4**, 140 (2020).

[54] D. Ortiz-Young, H. C. Chiu, S. Kim, K. Voïtchovsky, and E. Riedo, The interplay between apparent viscosity and wettability in nanoconfined water, Nat. Commun. **4**, 2482 (2013).

[55] O. Filippova and D. Hänel, Grid refinement for lattice-BGK models, J. Comput. Phys. **147**, 219 (1998).

[56] R. W. Mei, L. S. Luo, and W. Shyy, An accurate curved boundary treatment in the lattice Boltzmann method, J. Comput. Phys. **155**, 307 (1999).

[57] M. Bouzidi, M. Firdaouss, and P. Lallemand, Momentum transfer of a Boltzmann-lattice fluid with boundaries, Phys. Fluids **13**, 3452 (2001).

[58] P. Lallemand and L. S. Luo, Lattice Boltzmann method for moving boundaries, J. Comput. Phys. **184**, 406 (2003).

[59] A. Manacorda and A. Puglisi, Lattice Model to Derive the Fluctuating Hydrodynamics of Active Particles with Inertia, Phys. Rev. Lett. **119**, 208003 (2017).

[60] A. J. Ladd, Numerical simulations of particulate suspensions via a discretized Boltzmann equation. Part 1. Theoretical foundation, J. Fluid Mech. **271**, 285 (1994).

[61] C. K. Aidun, Y. Lu, and E. J. Ding, Direct analysis of particulate suspensions with inertia using the discrete Boltzmann equation, J. Fluid. Mech. **373**, 287 (1998).

[62] R. Mei, D. Yu, W. Shyy, and L. S. Luo, Force evaluation in the lattice Boltzmann method involving curved geometry, Phys. Rev. E **65**, 041203 (2002).

[63] P. Y. Huang, H. H. Hu, and D. D. Joseph, Direct simulation of the sedimentation of elliptic particles in Oldroyd-B fluids, J. Fluid Mech. **362**, 297 (1998).

[64] P. Y. Huang, J. Feng, and D. D. Joseph, The turning couples on an elliptic particle settling in a vertical channel, J. Fluid Mech. **271**, 1 (1994).

[65] A. Karnis, H. L. Goldsmith, and S. G. Mason, The flow of suspensions through tubes: V. Inertial effects, Can. J. Chem. Eng. **44**, 181 (1966).